The Journal of Chemical Physics

RESEARCH ARTICLE | MARCH 23 2026

Morphology, local stoichiometry, and photoexcited states in Cu@Cu_2O nanostructured systems grown by physical synthesis

Special Collection: Annabella Selloni Festschrift

Eleonora Spurio ; Francesca Alimonti ; Giovanni Bertoni ; Sergio D'Addato ; Giuseppe Ammirati ; Alessandra Paladini ; Stefano Turchini ; Daniele Catone ; Patrick O'Keeffe ; Paola Luches ✉

J. Chem. Phys. 164, 124702 (2026)
https://doi.org/10.1063/5.0309793

Articles You May Be Interested In

Comparative photocatalytic study of visible light driven $BiVO_4$, Cu_2O, and $Cu_2O/BiVO_4$ nanocomposite for degradation of antibiotic for wastewater treatment

J. Chem. Phys. (November 2023)

Efficient enhancement of hydrogen production by Ag/Cu_2O/ZnO tandem triple-junction photoelectrochemical cell

Appl. Phys. Lett. (March 2015)

Valence band offset of Cu_2O/In_2O_3 heterojunction determined by X-ray photoelectron spectroscopy

J. Appl. Phys. (October 2011)

The Journal
of Chemical Physics

ARTICLE

pubs.aip.org/aip/jcp

Morphology, local stoichiometry, and photoexcited states in $Cu@Cu_2O$ nanostructured systems grown by physical synthesis

Cite as: J. Chem. Phys. **164**, 124702 (2026); doi: 10.1063/5.0309793
Submitted: 29 October 2025 • Accepted: 5 March 2026 •
Published Online: 23 March 2026

Eleonora Spurio,[1] Francesca Alimonti,[1] Giovanni Bertoni,[1] Sergio D'Addato,[1,2] Giuseppe Ammirati,[3] Alessandra Paladini,[4] Stefano Turchini,[3] Daniele Catone,[3] Patrick O'Keeffe,[4] and Paola Luches[1,a)]

AFFILIATIONS

[1] CNR-Istituto Nanoscienze (CNR-NANO), Via G. Campi 213/a, 41125 Modena, Italy
[2] Dipartimento di Fisica Informatica e Matematica, Universitá di Modena e Reggio Emilia, 41121 Modena, Italy
[3] CNR-Istituto di Struttura della Materia (CNR-ISM), EuroFEL Support Laboratory (EFSL), Via del Fosso del Cavaliere 100, 00133 Rome, Italy
[4] CNR-Istituto di Struttura della Materia (CNR-ISM), EuroFEL Support Laboratory (EFSL), Monterotondo Scalo 00015, Italy

Note: This paper is part of the JCP Special Topic, Annabella Selloni Festschrift.
[a)] **Author to whom correspondence should be addressed:** paola.luches@nano.cnr.it

ABSTRACT

Cuprous oxide (Cu_2O) is a p-type semiconductor with promising applications as a photocathode material in photoelectrochemical cells for hydrogen production, owing to its visible-range bandgap and suitable band edge positions for water splitting. The incorporation of metallic Cu nanoparticles can further enhance light absorption and extend the absorption range of Cu_2O toward the red and near-infrared due to the excitation of localized surface plasmon resonances within the metal nanoparticles (NPs). Starting from molecular-beam-epitaxy-grown metallic Cu NPs, post-growth thermal treatments under oxidizing and reducing conditions can be tuned to obtain either $Cu@Cu_2O$ core@shell NPs or Cu_2O nanostructured films. The surface stoichiometry of the samples is investigated using x-ray photoelectron spectroscopy and Auger electron spectroscopy. Transmission electron microscopy, coupled with electron energy-loss spectroscopy, provides insights into the morphology and the local oxidation state of the NPs with nanometric resolution. Steady-state and time-resolved optical characterization of the samples confirms the presence of optical features related to localized surface plasmon resonances in the Cu cores and to exciton formation in the Cu_2O shell.

I. INTRODUCTION

In recent years, the increasing impact of climate change has significantly intensified the global demand for sustainable energy sources. Among the various strategies explored, photocatalytic water splitting is a promising approach to produce green hydrogen, a fuel with great potential for energy applications.[1,2] The photocatalytic process can be driven by a semiconductor-based photocatalyst, which interacts with solar light, generating electron–hole pairs. At the semiconductor/liquid interface, redox reactions occur that split water into hydrogen and oxygen.[1,2]

Copper oxides (Cu_2O and CuO) are interesting candidates as photoelectrocatalysts due to their favorable properties, including visible-range bandgap, non-toxicity, earth abundance, and suitable band edge positions for water splitting reactions.[3,4] Both are p-type semiconductors due to the low enthalpy of formation of Cu vacancies,[5,6] and they represent interesting materials to be used as photocathodes.[3,4,7] The optical response of Cu_2O is characterized by a complex excitonic structure arising from transitions between the two topmost valence bands of mainly Cu 3d character and the two lowest conduction bands of Cu 4s and 4p character. The yellow and green exciton series are due to the transitions between the bands of equal parity, and therefore, excitations to 1s excitonic states are dipole-forbidden; optical activity emerges from 2p excitonic states that give rise to weak transitions in the absorption spectrum between 2.2 and 2.6 eV. In contrast, the blue and violet series involve the bands of opposite parity, making their 1s excitons dipole-allowed and resulting in more intense absorption in the spectral region above 2.6 eV.[7–9] The material shows interesting optical properties linked to the formation of excitons with high binding energies above 100 meV.[10,11] On the contrary, CuO shows a narrower indirect bandgap of ~1.35 eV.[12] Despite these advantages, the photocatalytic efficiency of copper oxides is often hindered by photodegradation in aqueous environments and rapid recombination of electron–hole pairs, which typically occurs with a rate comparable to their migration rate to the photocatalyst surface, resulting in the loss of a significant portion of charge carriers before the reaction.[3]

The construction of a heterojunction photocatalyst offers an effective strategy to overcome this challenge by enabling spatial charge carrier separation.[3,13,14] The specific materials to be combined are a key factor in optimizing heterogeneous systems. In this context, previous studies have demonstrated that coupling metal oxides with metal nanoparticles (NPs) in the form of a core@shell structure can enhance photocatalytic performances.[15,16] Literature suggests that metal NPs can help to separate the photoexcited charges by acting as electron scavengers and increasing the lifetime of the photoexcited hole and the consequent photocatalytic activity.[17] In specific cases, the nanoparticles have a high extinction cross section via the excitation of localized surface plasmon resonances (LSPRs), coherent collective oscillations that occur when the incident light frequency matches the natural frequency of surface electrons that oscillate against the restoring force of positive nuclei.[18–20] After excitation, LSPRs can relax through energy or charge transfer to the surrounding medium.[19–23] By selecting plasmonic NPs with a resonance frequency that falls within the bandgap of the coupled semiconductor, it is also possible to extend the range of wavelengths absorbed by the system.[21–23] In addition, the shell typically protects the metallic core from oxidation and degradation.[24–26] Cu NPs are a promising alternative to more commonly used noble metals, such as Au and Ag, due to their low cost and ease of synthesis. Cu NPs exhibit a plasmonic resonance in the red/near-infrared region,[25,27] whereas copper oxide primarily absorbs in the visible range.

A dynamic description of the modifications occurring in composite materials upon photoexcitation is crucial to clarify the processes that take place and optimize the systems in view of achieving enhanced functionality. Femtosecond transient absorption spectroscopy (FTAS) is a powerful pump–probe technique, with a temporal resolution suitable to capture processes such as excited charge relaxation and transfer, occurring on timescales ranging from femtoseconds to picoseconds. The technique provides a time-resolved picture of the carrier population across the energy levels of the semiconductor upon bandgap photoexcitation.[21–23,28,29] On Cu oxide-based systems, the method has identified excitonic features in Cu_2O and direct bandgap-related features in CuO.[30]

The present work describes a procedure that allows us to stabilize $Cu@Cu_2O$ nanostructured films in a core@shell architecture. By finely tuning thermal treatments under oxidizing and reducing conditions, either Cu_2O nanostructured films or $Cu@Cu_2O$ core@shell systems can be obtained. The systems are characterized in local composition, in average surface stoichiometry, and in steady-state and transient optical absorption properties after photoexcitation above the bandgap of the oxide.

II. RESULTS AND DISCUSSION

A. Morphology and stoichiometry

The starting point to obtain core@shell NPs with a Cu core and a copper oxide shell is metallic Cu NPs of 6 nm equivalent thickness, deposited by molecular beam epitaxy (MBE) and annealed after the growth, as in our previous work.[31] The first step to obtain an oxide shell was a treatment in a furnace in O_2/N_2 flux at 373 K for 30 min. The resulting morphology is shown in the scanning transmission electron microscopy (STEM) image reported in Fig. 1(a), which shows the formation of irregularly shaped NPs with a bright core region and a dark shell. A statistical analysis of the NPs' size gives an average NP diameter of 23 nm, a core size of 15 nm, and a shell thickness of 4 nm (see Figs. S1 and S2 of the supplementary material). In many cases, the NPs show a darker area between the core and the shell, suggesting a different local density. To investigate the stoichiometry of the different morphological features, electron energy loss spectroscopy (EELS) maps were acquired on selected representative NPs and fitted with reference EELS spectra acquired on Cu, CuO, and Cu_2O reference samples, taken from Ref. 31.

The results of the analysis of an individual NP are shown in the inset of Fig. 1(a). The NP core is assigned to metallic Cu (cyan), while the shell region is composed mainly of Cu in the 1+ oxidation state that corresponds to the Cu_2O stoichiometry (magenta). The outermost layers of the shell show the prevalence of the Cu^{2+} component (green), ascribed to CuO.

To promote the reduction of the CuO component that contributes to the outermost layers to Cu_2O, a thermal treatment at 773 K in ultrahigh vacuum (UHV) for 30 min was performed. The morphology, as shown by the TEM image in Fig. 1(b), is not significantly modified, although the smallest NPs show a core region with a darker contrast than their shell. The smallest NPs probably undergo the Kirkendall effect,[32] which induces the full conversion of the metallic NP into a hollow oxide shell due to an unbalanced diffusion of O and Cu ions in the oxide. The same effect can also be observed in Fig. 1(a), where regions with darker contrast between the core and the shell are present in various NPs. The statistical analysis of the NP gives an average NP size of 34 nm, an average core size of 22 nm, and a shell size of 6 nm (see Fig. S3 of the supplementary material). The analysis of the EELS map of one of the largest NPs is shown in the inset of Fig. 1(b). In this case, the shell is entirely Cu_2O (magenta), while the core is metallic (cyan), and a dominant $Cu@Cu_2O$ architecture was obtained. The high temperature treatment reduces the oxide in the shell and induces a slightly larger average nanoparticle size, possibly due to the partial agglomeration of the smallest NPs (see Figs. S2 and S3 of the supplementary material).

The average EELS spectra before and after the reducing treatment are shown in Figs. 1(c) and 1(d). Expectedly, they appear as the superposition of EELS of a Cu^0 metallic phase and of a Cu^{1+} and Cu^{2+} phase (see also Ref. 31).

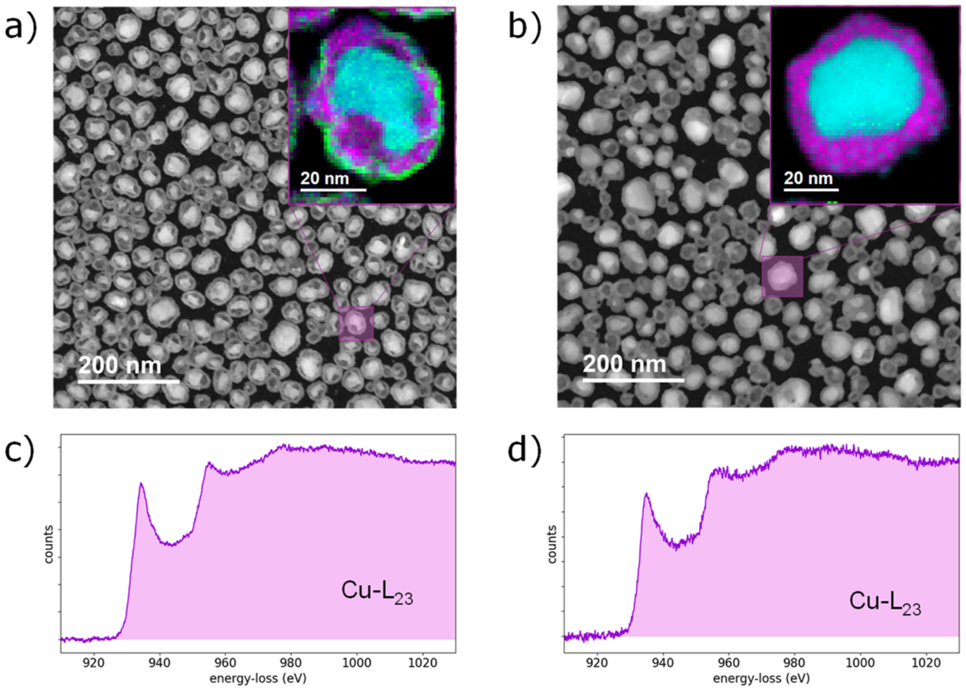

FIG. 1. (a) STEM image of Cu NPs annealed in an O_2/N_2 flux at 373 K for 30 min and (b) after annealing in UHV at 773 K for 60 min; insets of [(a) and (b)]: EELS maps of a single NP, in which the Cu^0 concentration is reported in cyan, the Cu^{1+} concentration is reported in magenta, and the Cu^{2+} concentration is reported in green. [(c) and (d)] Average Cu L_{23} EELS of [(a) and (b)], respectively.

TEM selected-area diffraction (SAED) patterns, reported in Fig. S8 of the supplementary material, confirm the assignment derived from EELS. Peaks related to a crystalline metallic phase and to a Cu_2O phase are visible both before and after the reduction treatment. Cu_2O-related peaks become more intense and narrower after the reduction treatment.

Figure 2 shows the results of the x-ray photoelectron spectroscopy (XPS) and Auger electron spectroscopy (AES) analysis of the sample shown in Fig. 1 after the two thermal treatments. The data provide information on the average surface stoichiometry to be compared with the results obtained by STEM-EELS, which offers high in-plane spatial resolution but is sensitive to the entire sample thickness in the out-of-plane direction. After the oxidation treatment in O_2/N_2, the Cu 2p XPS spectrum reported in Fig. 2(a) (green spectrum) shows two main peaks at 933 and 953 eV, related to emission from Cu $2p_{3/2}$ and $2p_{1/2}$ levels, respectively, with marked satellites on the high binding energy side of each peak. The presence of satellites, characteristic of the CuO stoichiometry,[33] demonstrates a non-negligible Cu^{2+} surface concentration, in agreement with the results obtained by STEM-EELS that show an outermost CuO layer on the NP shell. After the UHV annealing treatment (magenta spectrum), the main peaks appear much narrower, and the satellites lose most of their intensity, in agreement with the reduction of most of the external CuO layer to Cu_2O, observed by STEM-EELS. However, since metallic Cu and Cu_2O exhibit Cu 2p XPS peaks with a very similar shape and binding energy,[33] the presence of metallic Cu in the subsurface region cannot be excluded by the analysis of Cu 2p peaks. Cu $L_{23}M_{45}M_{45}$ AES spectra provide a higher sensitivity to the Cu oxidation state than the analysis of Cu 2p XPS spectra.[34]

Figure 2(b) shows the AES spectra of the sample after the two treatments. After oxidation in O_2/N_2, the AES peak appears rather broad and centered at 917.7 eV kinetic energy. The fit using

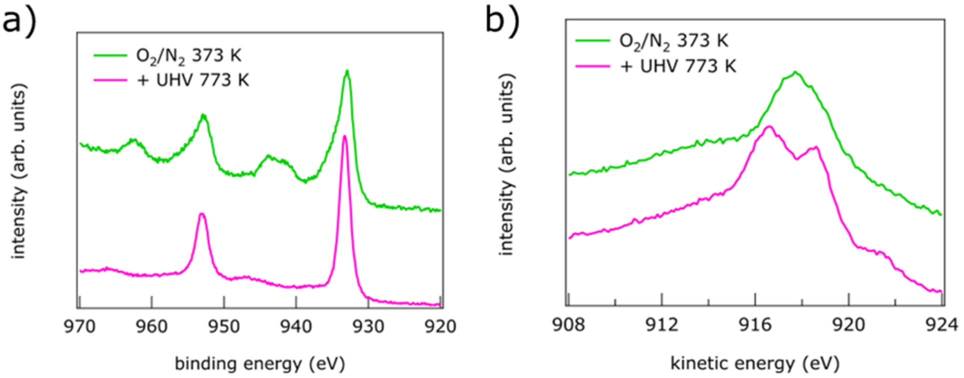

FIG. 2. (a) Cu 2p XPS *and* (b) Cu $L_{23}M_{45}M_{45}$ AES of the sample in Fig. 1 after oxidation in O_2/N_2 flux and after reduction in UHV.

TABLE I. Growth parameters for the four samples investigated: nominal Cu thickness, post-growth annealing temperature, oxidation temperature and time in O_2/N_2 flux, and UHV reduction temperature and time.

Sample	Thickness (nm)	T_{ox} (K)	t_{ox} (min)	T_{red} (K)	t_{red} (min)
$Cu@Cu_2O$ TEM	6	373	30	773	30
Cu_2O thin	2	423	40	623	30
Cu_2O thick	6	423	60	623	30
$Cu@Cu_2O$ FTAS	6	393	30	623	30

spectra from reference samples provides a Cu^{2+} concentration c_{Cu2+} = (60 ± 5)% and a Cu^{1+} concentration c_{Cu1+} = (40 ± 3)% [see Fig. S4(a) of the supplementary material]. After the reduction treatment in UHV, the spectrum shows two peaks at 918.6 and 916.6 eV kinetic energy, which correspond to metallic Cu and Cu_2O coming from the core and the shell of the NPs, respectively. The metallic component, detected by a surface sensitive technique such as AES, is possibly due to some partially uncovered NPs and/or non-uniform Cu_2O shells. The fit of the spectrum identifies a Cu^0 concentration c_{Cu0} = (45 ± 2)% and a Cu^{1+} concentration c_{Cu1+} = (55 ± 2)% [see Fig. S4(b) of the supplementary material].

Pure Cu_2O samples have also been grown as references. Starting from a 2 nm Cu equivalent thickness, using a slightly harsher oxidation treatment (423 K in O_2/N_2 flux for 40 min) and a milder reduction treatment (623 K in UHV for 30 min) as compared to the $Cu@Cu_2O$ NP sample (Table I), a sample with the morphology shown in the STEM image reported in Fig. 3(a) is obtained. Dense NPs with irregular shapes can be observed. The darker contrast core of the NPs shows that the NPs are hollow, as expected, because of the Kirkendall effect.[31,32] The average size of the NPs, identified via statistical analysis, is 21 nm, and the average shell thickness is 2.5 nm (see Fig. S5 of the supplementary material). No variation in the local stoichiometry is detected by STEM-EELS, with the average spectrum having the characteristic Cu^{1+} shape [Fig. 3(c)]. This spectrum appears different from those in Figs. 1(c) and 1(d) in the intensity of the L_2 and L_3 white lines and in their branching ratio.

A second Cu_2O sample with a 6 nm thickness was also grown to have a better signal to noise ratio in optical and FTAS spectra. It was treated as the 2 nm film with only a slightly longer oxidation treatment at 423 K in O_2/N_2 flux (Table I) to account for the larger thickness. The details of its morphology [Fig. 3(b)] are difficult to measure due to the presence of high-density interconnected grains of 7 nm average size (see Fig. S6 of the supplementary material) and to the possible superposition of grains over the surface that possibly decrease the contrast and do not allow us to clearly determine whether hollow shells are present.

Figure 3(d) shows the average Cu L_{23} EELS of the sample, consistent with a dominant Cu_2O stoichiometry, as in the case of the 2 nm sample [Fig. 3(c)].[31] UV–Vis spectrophotometry spectra and TEM-SAED patterns, reported in Figs. S7 and S8 of the supplementary material, respectively, confirm the dominant Cu_2O stoichiometry in the two samples.

To assess the surface composition, *in situ* XPS and AES characterization was performed (Fig. 4).

After the oxidation treatment for both samples, the Cu 2p XPS spectrum shows Cu $2p_{1/2}$ and $2p_{3/2}$ peaks at 953.5 and 933.7 eV binding energy, respectively, with marked satellites on the high binding energy side, typically observed in the CuO phase [Figs. 4(a) and 4(b)]. After the reduction treatment, the satellites lose most of their

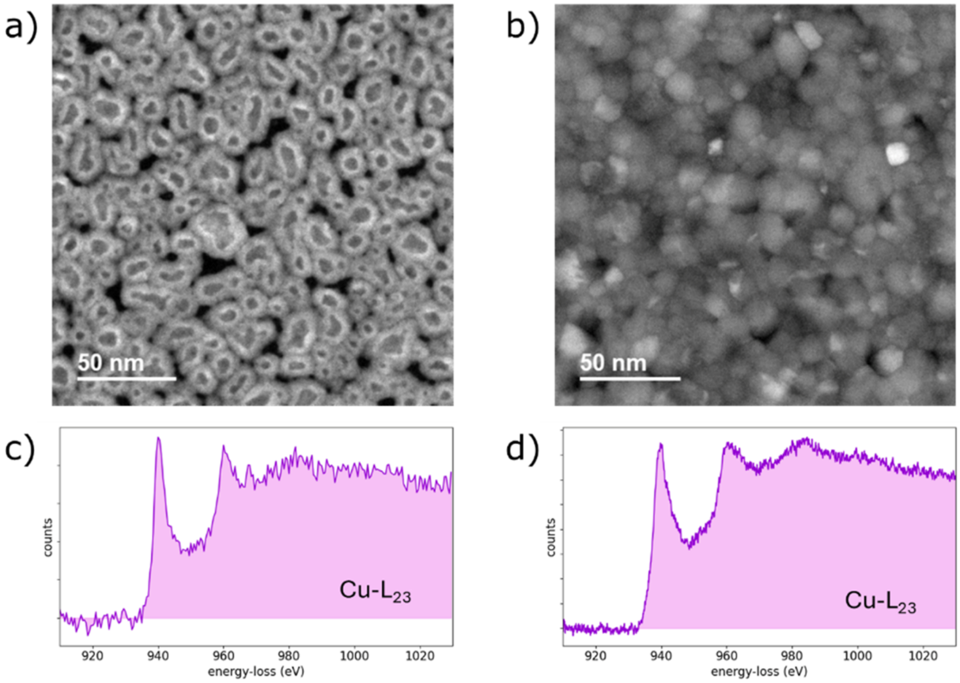

FIG. 3. STEM images of Cu_2O films with a thickness of 2 nm (a) and 6 nm (b) and corresponding average Cu L_{23} EELS [(c) and (d)].

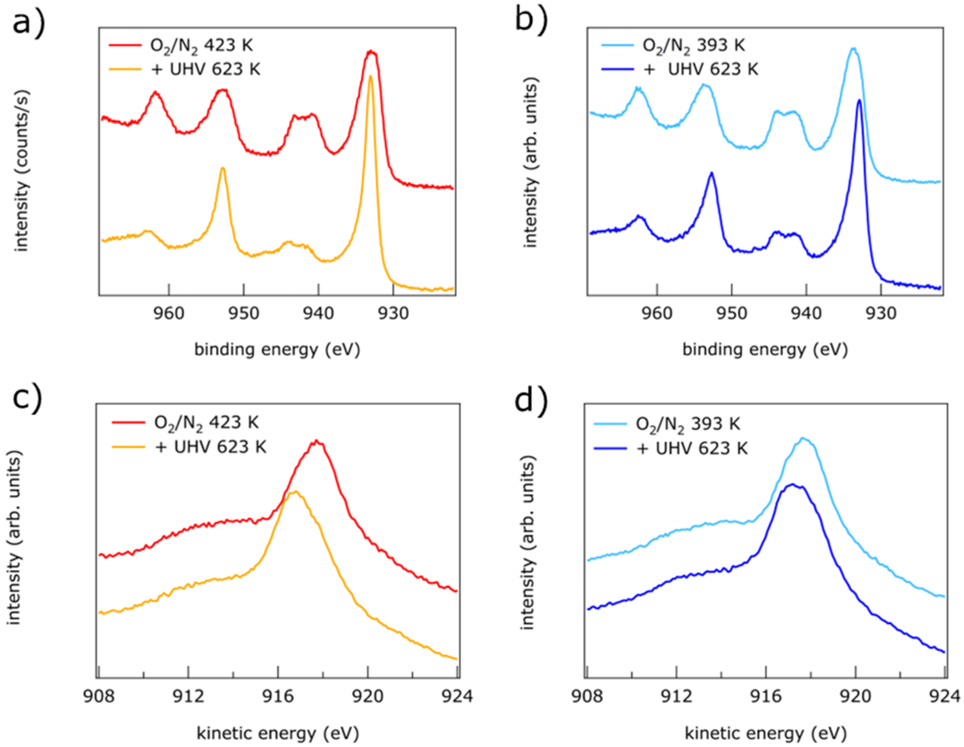

FIG. 4. Spectroscopic characterization of the 2 nm [(a) and (c)] and 6 nm [(b) and (d)] Cu_2O samples, after the oxidizing treatments in O_2/N_2 flux and after the reducing treatment in UHV: [(a) and (b)] Cu 2p XPS and [(c) and (d)] Cu $L_{23}M_{45}M_{45}$ AES.

intensity, and the main peaks appear again narrow and intense, in agreement with the reduction of most of the CuO phase to Cu_2O [Figs. 4(a) and 4(b)]. The Cu $L_{23}M_{45}M_{45}$ AES spectra shown in Figs. 4(c) and 4(d) confirm the assignment, with the spectrum after the oxidation treatment having a peak at 917.7 eV, assigned to a CuO stoichiometry, and the spectrum after the final reduction treatment having a peak at 916.8 eV, assigned to Cu_2O. The fit gives $c_{Cu1+} = (14 \pm 2)\%$ and $c_{Cu2+} = (86 \pm 7)\%$ for the 2 nm sample and $c_{Cu1+} = (12 \pm 2)\%$ and $c_{Cu2+} = (88 \pm 7)\%$ for the 6 nm sample [see Figs. S9(a) and S9(b) of the supplementary material]. After the reducing treatment, the Cu^{1+} concentration is significantly increased in both samples with $c_{Cu1+} = (66 \pm 3)\%$ and $c_{Cu2+} = (34 \pm 3)\%$ for the 2 nm sample and $c_{Cu1+} = (73 \pm 7)\%$ and $c_{Cu2+} = (27 \pm 3)\%$ for the 6 nm sample [see Figs. S9(c) and S9(d) of the supplementary material]. The comparison between the results obtained by XPS/AES and STEM-EELS indicates that in the Cu_2O samples, the Cu_2O stoichiometry is largely dominant and that the minority CuO phase is only present in the topmost layers to which electron spectroscopies are sensitive. The minor difference in Cu^{1+} concentration between the two samples may be attributed to their significantly different surface morphologies, which may host sites in which Cu^{1+} ions have a variable stability.

It has to be pointed out that the Cu^{1+} surface concentration does not change significantly after air exposure (see Fig. S10 of the supplementary material).

B. Optical characterization

An extensive optical characterization of the 6 nm Cu_2O sample and of a Cu@Cu_2O sample (Table I) was performed.

Figure 5(a) shows the absorption spectra of the Cu_2O and Cu@Cu_2O samples. The Cu_2O sample exhibits an absorption band in the 2.5–2.7 eV range [indicated by an arrow in Fig. 5(a)] that we have assigned to a possible overlap between the blue and violet exciton series, which, according to the literature, have transition energies of ~2.6 and 2.7 eV, respectively.[35] Below 2.4 eV, the absorption is at least an order of magnitude less, as the exciton transitions in this range have much weaker intensities (the yellow and green exciton series, measured at 77 K, are observed in the energy ranges of 2.0–2.2 and 2.2–2.3 eV, respectively).[36] The absorption spectrum of the Cu@Cu_2O sample also shows a similar absorption band above 2.2 eV, related to the formation of violet excitons in the Cu_2O shell—as evidenced by the change of slope at ~2.6 eV—and to interband transitions in metallic Cu.[27] The Cu@Cu_2O sample also shows an additional broad peak below 2.1 eV, centered at ~1.38 eV, which is ascribed to LSPR excitations in the metallic Cu cores, as previously observed in Cu@CuO_x NPs.[31,37] The absorption feature related to plasmonic resonances extends over a broader and redshifted energy range, as compared to the case of uniform dilute NPs.[38] An important observation is that there is no spectral overlap between the plasmonic transition of the Cu core and the excitonic transitions in the Cu_2O.

The absorption of the Cu@Cu_2O sample was simulated by boundary element method calculations[39] using the optical constants of Cu measured by Palik for Cu[40] and by Ito *et al.* for Cu_2O.[41] The experimental data are compared with the calculated extinction coefficient, given by the sum of the absorption and scattering cross sections. We considered individual nanostructures with three different shapes: a 22 nm diameter Cu nanosphere with a 6 nm thick Cu_2O

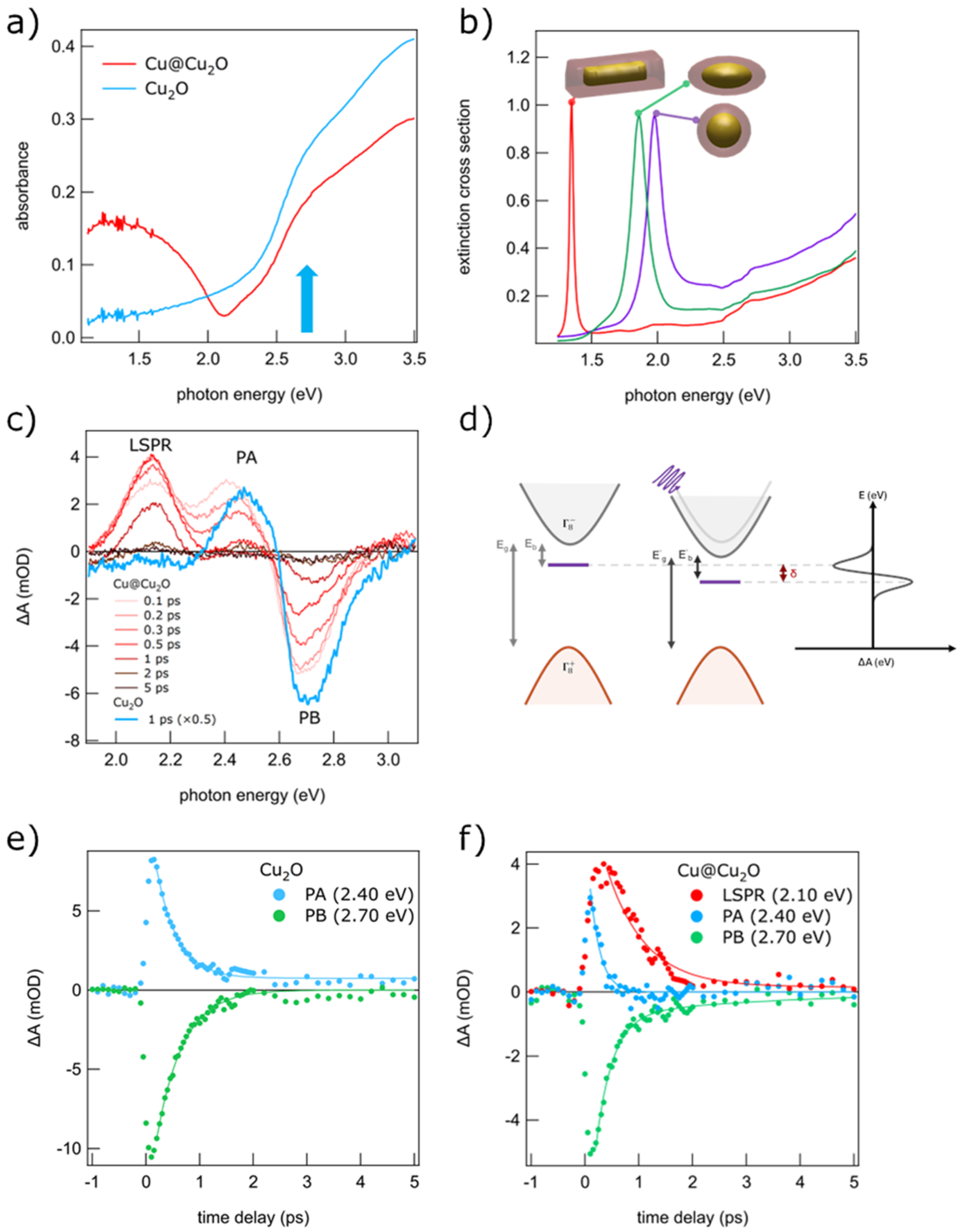

FIG. 5. (a) UV–Vis absorbance spectra of the Cu_2O and $Cu@Cu_2O$ samples; (b) simulation of the absorption coefficient for $Cu@Cu_2O$ core@shell NPs with different shapes; (c) TA spectra of the Cu_2O and $Cu@Cu_2O$ samples at selected delay times—pump 3.35 eV; (d) schematic illustration of the pump-induced perturbation of the band structure of an excitonic semiconductor material and the expected line shape of the transient absorption; (e) kinetic traces and fits of the PA (2.40 eV) and PB (2.70 eV) TA features of the Cu_2O sample—pump 3.35 eV; and (f) kinetic traces and fits of the LSPR (2.10 eV), PA (2.40 eV), and PB (2.70 eV) TA features of the $Cu@Cu_2O$ sample—pump 3.35 eV.

shell; a Cu prolate nanospheroid with major and minor axes of 22 and 11 nm, respectively, and a 6 nm thick Cu_2O shell; and a 40 × 10 × 10 nm^3 Cu nanobar with a Cu_2O shell giving a 60 × 20 × 20 nm^3 external size. The edges of the nanobar are rounded with profiles of radius 3 nm to more realistically simulate the actual geometries and to avoid spurious effects due to sharp edges. The simulations, reported in Fig. 5(b), show that the energy of the plasmonic resonance is significantly shifted to lower energy with increasing aspect ratio of the particles. The broad LSPR resonance band observed in the experimental absorption spectrum of $Cu@Cu_2O$ in Fig. 5(a) can, therefore, be ascribed to the broad distribution of particle sizes that results in a broad distribution of aspect ratios.[31] In addition, given their proximity, the NPs also possibly interact with each other, resulting in absorption at even lower energies than in bare metallic and Cu_2O covered Cu NPs.[31,42]

Figure 5(c) shows the transient absorption (TA) spectra acquired with a pump at a photon energy of 3.35 eV: the Cu_2O TA spectrum at 1 ps (thick blue line), shown as a reference, and the $Cu@Cu_2O$ TA spectra at selected time delays (0.1, 0.2, 0.3, 0.5, 1.0, 2.0, and 5.0 ps). The Cu_2O TA spectrum presents two main features: (i) a negative peak corresponding to a photobleaching (PB) signal centered at 2.70 eV, and (ii) a positive peak corresponding to photoinduced absorption (PA) centered at 2.46 eV. We suggest that both the PB and PA signals arise from the same perturbation of the excitonic transition observed in the steady state absorption. The effect of photoexcitation is to induce an energy shift of the exciton resonance due to the competing effects of bandgap renormalization and exciton screening. Figure 5(d) shows a schematic illustration of these effects in which E_g and E_b are the electronic bandgap and the exciton binding energy in steady state conditions; E'_g and E'_b are the electronic bandgap and the exciton binding energy after pump excitation, and δ indicates the total shift of the excitonic resonance. This is in agreement with the literature descriptions of the transient absorption of strongly excitonic materials[43,44] but contrasts with previous works on ultrafast spectroscopy of Cu_2O in which the PB and PA are assigned to separate ground-state bleaching and excited-state absorptions.[30] However, we point out that this derivative-like spectral line shape with a zero-crossing corresponding to the excitonic energy transition (2.6 eV) in the steady state absorption spectrum is characteristic of the transient optical response of excitonic materials.[43,44] The TA spectra of the Cu@Cu_2O sample also show the characteristic PB and PA signals (centered at ~2.70 and ~2.40 eV, respectively) observed in the case of the Cu_2O sample, which we have assigned to the perturbation of the excitonic transition by photoexcitation in the material. In addition, a broad positive signal centered at 2.12 eV is observed, which we assign to the positive wing of the transient modification of the plasmonic resonance. In the case of Cu NPs, the pump induces a broadening and a decrease of the central intensity of the plasmon resonance, giving rise to a transient spectrum with a negative feature at the energy of the plasmon resonance and to positive features in the wings of the plasmon resonance.[45] This TA spectral line shape is due to changes in the complex dielectric function of the metal following photoexcitation.[21,22] Here, we only observe the high-energy positive wing of the full TA feature due to the limited range of the white light used as a probe. As already mentioned in the case of the steady state absorption spectrum, also in the TA spectra, the transient signals due to the modification of the plasmonic resonance of the Cu core and the excitonic transition of the Cu_2O are spectrally separated, with only a minor overlap between the PA and LSPR features.

The temporal dynamics of the principal features of the TA spectra of the Cu_2O [Fig. 5(e)] and of the Cu@Cu_2O [Fig. 5(f)] samples were analyzed by fitting with exponential decay functions. In particular, the fast dynamics of the excitonic features in the Cu_2O sample for both PA (2.40 eV) and PB (2.70 eV) signals gives a decay constant of (480 ± 50) fs, which is comparable with the experimental results reported in the literature for bare Cu_2O.[30] The signal kinetics are largely independent of probe energy across the positive (PA) and negative (PB) features, suggesting that their decay dynamics arise from the same mechanism. On the other hand, the Cu@Cu_2O sample shows a decay time of (450 ± 50) fs for the PB feature (2.70 eV), in agreement with bare Cu_2O, whereas the PA feature (2.40 eV) exhibits a shorter decay time of (160 ± 50) fs. Here, we suggest that the faster dynamics of the PA in the Cu@Cu_2O sample, compared either to the PA in the Cu_2O sample or to the LSPR response of the Cu@Cu_2O sample, may arise from additional contributions associated with electron thermalization processes in the Cu core following above-bandgap photoexcitation. Indeed, previous studies have shown that non-thermalized electrons in plasmonic nanoparticles can exhibit a markedly different spectral response during the first few hundred femtoseconds after photoexcitation compared to that of thermalized electrons.[46,47] The kinetics of the PB feature (2.70 eV), which is spectrally well separated from the LSPR feature in the Cu@Cu_2O sample, is the same in Cu_2O and Cu@Cu_2O samples. Conversely, the LSPR signal (2.10 eV) exhibits slower decay dynamics with a characteristic time of (710 ± 40) fs, typical of the relaxation pathways in Cu NPs, where electron–electron and electron–phonon scattering processes dissipate the plasmonic energy into the lattice.[48] The above measured decay time is only slightly larger than those reported for interband-excited Cu nanorods (565 fs)[48] and 30 nm nanospheres (510 fs).[49] This suggests that the electron–phonon coupling dynamics is not significantly influenced by size in Cu nanostructures above a few tens of nm. The spectral separation of the plasmonic and negative excitonic features has allowed us to measure the decay times of the metal core and semiconductor shell independently. This situation contrasts with the case of the Cu_2O core and Cu shell system, where the plasmonic resonance of the metallic shell overlaps with the excitonic resonance of the oxide.[45] The PB trace also shows a very weak signal at longer decay times, which does not permit us to extract reliable information. Such long lasting kinetics was ascribed to defect trapping in a previous study.[30]

Steady-state and time-resolved optical results show that the Cu@Cu_2O sample combines the unique characteristic optical features of Cu_2O in the visible region and those of metallic Cu NPs in the red/near-infrared region. The intense LSPR-related absorption indicates that the core@shell morphology not only extends the absorption range, but also preserves the metallic core from oxidation, in line with the results obtained by TEM (Fig. 1), while bare Cu NPs exposed to air typically show only rather weak plasmonic resonances.[50] Furthermore, the present results indicate that the oxidation of the Cu_2O shell to CuO is not significant, since the characteristic optical features of CuO[30] are not observed in either the steady-state or time-resolved spectra.

III. CONCLUSIONS

Composite systems made of cuprous oxide coupled with Cu NPs can be obtained by physical synthesis methods. The formation of pure Cu_2O nanostructured films or core@shell Cu@Cu_2O NPs depends on the temperature of the post-growth oxidation and reduction treatments. TEM combined with STEM-EELS and XPS/AES spectroscopies was used to identify a procedure to obtain the desired Cu@Cu_2O morphology by following the effect of various treatments. Mild oxidation treatments at 373–393 K are necessary to partially oxidize the outer layers of the metallic Cu NPs to a mixture of CuO and Cu_2O, with CuO mainly present on the surface. A reduction in UHV above 623 K leads to a dominant Cu_2O shell stoichiometry. Longer thermal oxidation treatments at a higher temperature of 423 K, followed by reducing treatments in UHV at 623 K, lead to nanostructured films with dominant Cu_2O stoichiometry. Steady-state and time-resolved optical spectroscopies have shown that the Cu@Cu_2O samples combine a stable plasmonic Cu metal core and a protective Cu_2O shell with excitonic properties.

IV. MATERIALS AND METHODS

A. Sample preparation

The samples examined in this work were grown using MBE, a bottom-up deposition technique operating under UHV conditions. The UHV ($P \sim 10^{-10}$ mbar) setup consists of two interconnected chambers: one dedicated to MBE growth and the other for *in situ* XPS, AES characterization, and UHV annealing treatments.

The samples for TEM characterization were deposited on a Si microchip with 15 nm thick electron transparent silicon nitride windows. The TEM microchips were cleaned using plasma treatment for 3 minutes at 40% power before sample deposition. For XPS/AES, optical, and FTAS characterization, the samples were deposited on UV-grade fused silica substrates. These substrates were pre-cleaned in boiling acetone for 5 minutes and subsequently treated in an ultrasonic bath—first in boiling acetone and then in boiling isopropanol—for 3 min each. To remove residual surface contaminants and ensure high-quality deposition, all substrates were annealed in UHV at 773 K for 15 min before deposition.

Cu was evaporated from a Knudsen cell held at 1453 K. Cu atoms self-assembled on the substrate, forming Cu NPs. The nominal thickness of each sample was estimated using the Cu deposition rate, which was measured before growth using a quartz crystal microbalance.

Different post-growth treatments in UHV and in a quartz tube furnace in 50% N_2 and 50% O_2 flux were performed to obtain Cu_2O and Cu@Cu_2O. The treatments undergone by each sample are summarized in Table I.

B. XPS and AES characterization

The chemical composition of the sample surface was investigated *in situ* by XPS and AES, using Al Kα (1486.6 eV) radiation and a hemispherical analyzer with a pass energy of 30 eV. To obtain the surface concentration of the different Cu ionic species, the AES spectra were fit using a linear combination of spectra measured on reference Cu, CuO, and Cu_2O samples.[31] The uncertainties associated with the concentrations of the different Cu ionic species were derived from the standard deviations of the fitting parameters.

C. UV–Vis spectrophotometry characterization

The optical properties of the systems were studied using UV–Vis absorption spectroscopy. The spectrometer setup consists of a xenon lamp, a monochromator, a linear polarizer, a silicon photodetector, and a picoammeter. The sample holder was positioned so that the sample surface formed an angle of 22° with the incident beam. The absorbance (A) spectrum was calculated from the collected transmittance (T) and reflectance (R) signals using the relation $A = 1 - T - R$. The optical absorption spectrum of the Cu@Cu_2O sample was simulated via a boundary element method,[39] using the optical constants from Palik for Cu[40] and from Ito *et al.* for Cu_2O.[41]

D. FTAS characterization

The FTAS measurements were performed at the EFSL laboratories of CNR-ISM. The experimental setup employs an amplified femtosecond laser system delivering 35 fs pulses at a 1 kHz repetition rate, with an average power of 4 W centered at 800 nm. Tunable pump pulses are generated using an optical parametric amplifier. A pump wavelength of 3.35 eV and a pump fluence of 660 μJ/cm^2 were used for the present study. The probe beam is either a visible white-light supercontinuum (1.60–3.45 eV), produced by focusing 3 μJ of the 800 nm laser pulse into a rotating CaF_2 crystal, or an IR supercontinuum (0.82–1.38 eV), generated by focusing the 800 nm laser into a 3 mm YAG crystal. The pump and probe beams are focused on the sample with spot diameters of ~200 and 150 μm, respectively. The delay time between the two beams is controlled by adjusting the optical path length of the probe, yielding an instrument response function of about 50 fs. More detailed information about the setup can be found elsewhere.[28,51]

E. TEM characterization

TEM was employed to investigate the morphology of the samples using a ThermoFisher Talos FS200, equipped with a Schottky gun operating at 200 kV. STEM in the dark-field mode (ADF-STEM) was used to investigate the sample morphology. EELS in the STEM mode, with an analytical probe of ~0.5 nm, was used to acquire spectral images to determine the sample's local stoichiometry. In particular, the Cu L_{23} edge at 920–980 eV was used to determine the local oxidation state of Cu within the nanoparticles. Statistical analysis of the STEM images was performed using machine learning algorithms implemented in the Python libraries *sklearn* and *skimage*. The method is sketched in Fig. S1 of the supplementary material. The STEM images were first segmented by intensity using a *kMeans* algorithm to obtain three binary masks for the background, shell, and core. The particles were subsequently separated using a standard watershed algorithm applied to the sum of the core and shell masks. The equivalent diameters of the NPs were evaluated and analyzed using a Gaussian mixture model to account for possible multimodal distributions, providing a quantitative description of the particle size dispersion. The local thickness of the shell region was statistically determined for each particle from the shell mask, provided that a core was detected in the corresponding core mask. The chemical maps of individual particles were obtained by fitting the Cu L_{23}-edge spectral images with a linear combination of three reference spectra for Cu^0, Cu^{1+}, and Cu^{2+}, taken from Ref. 31, plus a power-law function to account for the spectrum background. The four fitted coefficients were used to obtain the concentration of the three different Cu components at each spatial position in the spectral image.

SUPPLEMENTARY MATERIAL

The supplementary material includes the statistical analysis of TEM images and the fittings of the AES spectra.

ACKNOWLEDGMENTS

This work was supported by the European Union–NextGenerationEU (NGEU) Mission 4, Component 2, National Sustainable Mobility Center Grant No. CN00000023; the Italian Ministry of University and Research, Decree No. 1033 (June 17, 2022), Spoke 11, Innovative Materials and Lightweighting; and the Ministero dell'Istruzione, dell'Università e della Ricerca (MIUR) Grant Nos. PRIN 2022 PNRR ResET P2022ZHCT3 CUP: B53D23028720001 and PRIN 2022 e-DYNAFOX 2022YXJ55F CUP: B53C24006290006. G.A. acknowledges the funding from the European Union–NextGenerationEU (NGEU) Mission 4, Component 2, PNRR Project No. NFFA-DI IR0000015, CUP:

B53C22004310006. G.B. acknowledges the funding from the European Union–NextGenerationEU (NGEU) Mission 4, Component 2, PNRR Project No. IR0000027 iENTRANCE@ENL, CUP: B33C22000710006.

AUTHOR DECLARATIONS

Conflict of Interest

The authors have no conflicts to disclose.

Author Contributions

Eleonora Spurio: Conceptualization (supporting); Data curation (lead); Formal analysis (lead); Investigation (equal); Methodology (equal); Supervision (supporting); Validation (supporting); Visualization (equal); Writing – review & editing (supporting). **Francesca Alimonti**: Data curation (supporting); Formal analysis (supporting); Investigation (supporting); Visualization (supporting); Writing – original draft (supporting); Writing – review & editing (supporting). **Giovanni Bertoni**: Data curation (equal); Formal analysis (equal); Investigation (equal); Methodology (equal); Software (lead); Validation (equal); Writing – review & editing (supporting). **Sergio D'Addato**: Conceptualization (supporting); Methodology (supporting); Supervision (supporting); Writing – review & editing (supporting). **Giuseppe Ammirati**: Data curation (equal); Formal analysis (equal); Investigation (equal); Methodology (equal); Software (supporting); Writing – review & editing (equal). **Alessandra Paladini**: Data curation (equal); Formal analysis (equal); Investigation (equal); Methodology (equal); Writing – review & editing (equal). **Stefano Turchini**: Conceptualization (supporting); Funding acquisition (equal); Methodology (equal); Project administration (equal); Validation (equal); Writing – review & editing (equal). **Daniele Catone**: Conceptualization (equal); Data curation (equal); Formal analysis (equal); Investigation (equal); Methodology (equal); Validation (equal); Writing – review & editing (equal); **Patrick O'Keeffe**: Conceptualization (equal); Funding acquisition (equal); Investigation (equal); Methodology (equal); Project administration (equal); Validation (equal); Writing – review & editing (equal). **Paola Luches**: Conceptualization (lead); Funding acquisition (equal); Methodology (equal); Project administration (equal); Resources (lead); Supervision (lead); Validation (lead); Visualization (equal); Writing – original draft (lead); Writing – review & editing (equal).

DATA AVAILABILITY

The data that support the findings of this study are available from the corresponding author upon reasonable request.

REFERENCES

[1] K. Maeda, "Photocatalytic water splitting using semiconductor particles: History and recent developments," J. Photochem. Photobiol., C **12**(4), 237–268 (2011).

[2] K. Villa, J. R. Galán-Mascarós, N. López, and E. Palomares, "Photocatalytic water splitting: Advantages and challenges," Sustainable Energy Fuels **5**(18), 4560–4569 (2021).

[3] A. Paracchino, V. Laporte, K. Sivula, M. Grätzel, and E. Thimsen, "Highly active oxide photocathode for photoelectrochemical water reduction," Nat. Mater. **10**(6), 456–461 (2011).

[4] J. Li, X. Jin, R. Li, Y. Zhao, X. Wang, X. Liu, and H. Jiao, "Copper oxide nanowires for efficient photoelectrochemical water splitting," Appl. Catal. B: Environ. **240**, 1–8 (2019).

[5] M. Nolan and S. D. Elliott, "The p-type conduction mechanism in Cu_2O: A first principles study," Phys. Chem. Chem. Phys. **8**(45), 5350–5358 (2006).

[6] H. Raebiger, S. Lany, and A. Zunger, "Origins of the *p*-type nature and cation deficiency in Cu_2O and related materials," Phys. Rev. B **76**(4), 045209 (2007).

[7] B. K. Meyer, A. Polity, D. Reppin, M. Becker, P. Hering, P. J. Klar, T. Sander, C. Reindl, J. Benz, M. Eickhoff, C. Heiliger, M. Heinemann, J. Bläsing, A. Krost, S. Shokovets, C. Müller, and C. Ronning, "Binary copper oxide semiconductors: From materials towards devices," Physica Status Solidi B **249**(8), 1487–1509 (2012).

[8] M. Heinemann, B. Eifert, and C. Heiliger, "Band structure and phase stability of the copper oxides Cu_2O, CuO, and Cu_4O_3," Phys. Rev. B **87**(11), 115111 (2013).

[9] M. Takahata and N. Naka, "Photoluminescence properties of the entire excitonic series in Cu_2O," Phys. Rev. B **98**, 195205 (2018).

[10] J. T. Warren, K. E. O'Hara, and J. P. Wolfe, "Two-body decay of thermalized excitons in Cu_2O," Phys. Rev. B **61**(12), 8215–8223 (2000).

[11] V. T. Agekyan, "Spectroscopic properties of semiconductor crystals with direct forbidden energy gap," Physica Status Solidi A **43**(1), 11–42 (1977).

[12] F. P. Koffyberg and F. A. Benko, "A photoelectrochemical determination of the position of the conduction and valence band edges of *p*-type CuO," J. Appl. Phys. **53**(2), 1173–1177 (1982).

[13] J. Zhang, H. Ma, and Z. Liu, "Highly efficient photocatalyst based on all oxides WO_3/Cu_2O heterojunction for photoelectrochemical water splitting," Appl. Catal. B: Environ. **201**, 84–91 (2017).

[14] J. Luo, L. Steier, M.-K. Son, M. Schreier, M. T. Mayer, and M. Grätzel, "Cu_2O nanowire photocathodes for efficient and durable solar water splitting," Nano Lett. **16**(3), 1848–1857 (2016).

[15] C. Clavero, "Plasmon-induced hot-electron generation at nanoparticle/metal-oxide interfaces for photovoltaic and photocatalytic devices," Nat. Photonics **8**(2), 95–103 (2014).

[16] V. Navakoteswara Rao, N. Lakshmana Reddy, V. Preethi, M. Karthik, Y.-T. Yu, J. M. Yang, M. Mamatha Kumari, and M. V. Shankar, "A critical review on core/shell-based nanostructured photocatalysts for improved hydrogen generation," Int. J. Hydrogen Energy **48**(31), 11754–11774 (2023).

[17] M. A. Mahmoud, W. Qian, and M. A. El-Sayed, "Following charge separation on the nanoscale in Cu_2O–Au nanoframe hollow nanoparticles," Nano Lett. **11**(8), 3285–3289 (2011).

[18] A. Amirjani, N. B. Amlashi, and Z. S. Ahmadiani, "Plasmon-enhanced photocatalysis based on plasmonic nanoparticles for energy and environmental solutions: A review," ACS Appl. Nano Mater. **6**(11), 9085–9123 (2023).

[19] N. Wu, "Plasmonic metal-semiconductor photocatalysts and photoelectrochemical cells: A review," Nanoscale **10**(6), 2679–2696 (2018).

[20] J. Li, S. K. Cushing, J. Bright, F. Meng, T. R. Senty, P. Zheng, A. D. Bristow, and N. Wu, "Ag@Cu_2O core-shell nanoparticles as visible-light plasmonic photocatalysts," ACS Catal. **3**(1), 47–51 (2013).

[21] J. S. Pelli Cresi, M. C. Spadaro, S. D'Addato, S. Valeri, S. Benedetti, A. Di Bona, D. Catone, L. Di Mario, P. O'Keeffe, A. Paladini, G. Bertoni, and P. Luches, "Highly efficient plasmon-mediated electron injection into cerium oxide from embedded silver nanoparticles," Nanoscale **11**(21), 10282–10291 (2019).

[22] E. Spurio, J. S. Pelli Cresi, G. Ammirati, S. Pelatti, A. Paladini, S. D'Addato, S. Turchini, P. O'Keeffe, D. Catone, and P. Luches, "Injecting Electrons into CeO_2 via Photoexcitation of Embedded Au Nanoparticles," ACS Photonics **10**(5), 1566–1574 (2023).

[23] D. C. Ratchford, A. D. Dunkelberger, I. Vurgaftman, J. C. Owrutsky, and P. E. Pehrsson, "Quantification of efficient plasmonic hot-electron injection in gold Nanoparticle–TiO_2 films," Nano Lett. **17**(10), 6047–6055 (2017).

[24] S. D'Addato, M. Lanza, A. Boiani, E. Spurio, S. Pelatti, G. Paolicelli, and P. Luches, "Morphology and optical properties of gas-phase-synthesized plasmonic nanoparticles: Cu and Cu/MgO," Materials **15**, 4429 (2022).

[25] E. Spurio, S. Pelatti, S. D'Addato, and P. Luches, "Plasmonic properties and stability of Au and Cu nanoparticles embedded in cerium oxide," J. Phys.: Condens. Matter **36**(37), 375003 (2024).

[26] P. C. D. Mendes, Y. Song, W. Ma, T. Z. H. Gani, K. H. Lim, S. Kawi, and S. M. Kozlov, "Opportunities in the design of metal@oxide core-shell nanoparticles," Adv. Phys.: X **8**(1), 2175623 (2023).

[27] C. Lee, Y. Park, and J. Y. Park, "Hot electrons generated by intraband and interband transition detected using a plasmonic Cu/TiO_2 nanodiode," RSC Adv. **9**(32), 18371–18376 (2019).

[28] D. Catone, L. Di Mario, F. Martelli, P. O'Keeffe, A. Paladini, J. Stefano Pelli Cresi, A. K. Sivan, L. Tian, F. Toschi, and S. Turchini, "Ultrafast optical spectroscopy of semiconducting and plasmonic nanostructures and their hybrids," Nanotechnology **32**(2), 025703 (2020).

[29] T.-H. Lai, K.-i. Katsumata, and Y.-J. Hsu, "In situ charge carrier dynamics of semiconductor nanostructures for advanced photoelectrochemical and photocatalytic applications," Nanophotonics **10**(2), 777–795 (2020).

[30] L. Shenje, S. Larson, Y. Zhao, and S. Ullrich, "Composition effects on ultrafast optical properties of Cu_xO_y thin films: A transient absorption study," J. Phys. Chem. C **124**(45), 24908–24918 (2020).

[31] E. Spurio, G. Bertoni, S. D'Addato, F. Alimonti, and P. Luches, "Mapping the local stoichiometry in Cu nanoparticles during controlled oxidation by STEM-EELS spectral imaging," Nanoscale **17**(7), 4132–4141 (2025).

[32] A. D. Smigelskas and E. O. Kirkendall, *Zinc Diffusion in Alpha Brass* (The American Institute of Mining, Metallurgical, and Petroleum Engineers, 1946).

[33] D. Tahir and S. Tougaard, "Electronic and optical properties of Cu, CuO and Cu_2O studied by electron spectroscopy," J. Phys.: Condens. Matter **24**(17), 175002 (2012).

[34] M. C. Biesinger, "Advanced analysis of copper x-ray photoelectron spectra," Surf. Interface Anal. **49**(13), 1325–1334 (2017).

[35] S. Brahms and S. Nikitine, "Intrinsic absorption and reflection of cuprous oxide in the 2.5 to 6.5 eV region," Solid State Commun. **3**(8), 209–212 (1965).

[36] E. F. Gross, "Optical spectrum of excitons in the crystal lattice," Il Nuovo Cimento **3**(S4), 672–701 (1956).

[37] T. Ghodselahi and M. A. Vesaghi, "Localized surface plasmon resonance of Cu@Cu_2O core–shell nanoparticles: Absorption, scattering and luminescence," Physica B **406**(13), 2678–2683 (2011).

[38] V. N. Popok, S. M. Novikov, Y. Y. Lebedinskij, A. M. Markeev, A. A. Andreev, I. N. Trunkin, A. V. Arsenin, and V. S. Volkov, "Gas-aggregated copper nanoparticles with long-term plasmon resonance stability," Plasmonics **16**(2), 333–340 (2021).

[39] U. Hohenester and A. Trügler, "MNPBEM—A Matlab toolbox for the simulation of plasmonic nanoparticles," Comput. Phys. Commun. **183**(2), 370–381 (2012).

[40] E. D. Palik, *Handbook of Optical Constants of Solids* (Academic Press, San Diego, California, 1985).

[41] T. Ito, T. Kawashima, H. Yamaguchi, T. Masumi, and S. Adachi, "Optical properties of Cu_2O studied by spectroscopic ellipsometry," J. Phys. Soc. Jpn. **67**(6), 2125–2131 (1998).

[42] P. K. Jain and M. A. El-Sayed, "Plasmonic coupling in noble metal nanostructures," Chem. Phys. Lett. **487**(4–6), 153–164 (2010).

[43] G. Ammirati, F. Martelli, P. O'Keeffe, S. Turchini, A. Paladini, M. Palummo, G. Giorgi, M. Cinquino, M. De Giorgi, L. De Marco, and D. Catone, "Band structure and exciton dynamics in Quasi-2D dodecylammonium halide perovskites," Adv. Opt. Mater. **11**(7), 2201874 (2023).

[44] E. A. A. Pogna, M. Marsili, D. De Fazio, S. Dal Conte, C. Manzoni, D. Sangalli, D. Yoon, A. Lombardo, A. C. Ferrari, A. Marini, G. Cerullo, and D. Prezzi, "Photo-induced bandgap renormalization governs the ultrafast response of single-layer MoS_2," Acs Nano **10**(1), 1182–1188 (2016).

[45] M. Tariq, M. D. Koch, J. W. Andrews, and K. E. Knowles, "Correlation between surface chemistry and optical properties in colloidal Cu_2O nanoparticles," J. Phys. Chem. C **124**(8), 4810–4819 (2020).

[46] P. O'Keeffe, D. Catone, L. Di Mario, F. Toschi, M. Magnozzi, F. Bisio, A. Alabastri, R. Proietti Zaccaria, A. Toma, G. Della Valle, and A. Paladini, "Disentangling the temporal dynamics of nonthermal electrons in photoexcited gold nanostructures," Laser Photonics Rev. **15**(6), 2100017 (2021).

[47] P. O'Keeffe, G. Ammirati, D. Catone, J. S. Pelli Cresi, F. Toschi, M. Magnozzi, G. Della Valle, F. Bisio, and A. Paladini, "Ultrafast dynamics of nonthermal carriers following plasmonic and interband photoexcitation of 2D arrays of gold nanoparticles," ACS Photonics **11**(8), 3205–3212 (2024).

[48] B. T. Diroll, S. Jeong, and X. Ye, "Ultrafast dynamics of colloidal copper nanorods: Intraband versus interband excitation," Small Science **2**(3), 2100103 (2022).

[49] Q. Darugar, W. Qian, M. A. El-Sayed, and M.-P. Pileni, "Size-dependent ultrafast electronic energy relaxation and enhanced fluorescence of copper nanoparticles," J. Phys. Chem. B **110**(1), 143–149 (2006).

[50] Y. Fang, Z. Cheng, S. Wang, H. Hao, L. Li, S. Zhao, X. Chu, and R. Zhu, "Effects of oxidation on the localized surface plasmon resonance of Cu nanoparticles fabricated via vacuum coating," Vacuum **184**, 109965 (2021).

[51] V. Campanari, D. Catone, P. O'Keeffe, A. Paladini, S. Turchini, F. Martelli, M. Salvato, N. Loudhaief, E. Campagna, and P. Castrucci, "Dynamics of the bulk-to-topological state scattering of photoexcited carriers in Bi_2Se_3 thin films," ACS Appl. Electron. Mater. **5**(8), 4643–4649 (2023).